Hand Gesture Recognition Using Three-Dimensional Electrical Impedance Tomography

Dai Jiang, *Member, IEEE*, Yu Wu, *Member, IEEE*, and Andreas Demosthenous, *Fellow, IEEE*

Abstract—This brief presents a 16-electrode electrical impedance tomography (EIT) system for hand gesture recognition. The hardware of the system is based on integrated circuits including a 12-bit high spectral purity current-steering DAC implemented in 0.18 μm CMOS technology, a current driver and an instrumentation amplifier in 0.35 μm CMOS technology. Both 2D and 3D EIT electrode arrangements were tested for hand gesture recognition. It is shown that using machine learning algorithms, eight hand gestures can be distinguished from the measured bio-impedance data with an accuracy of 97.9% when the electrodes are placed on a single wristband, and an accuracy of 99.5% with the same number of electrodes distributed on two wristbands for 3D EIT measurement. In particular 3D EIT demonstrated significant superiority in its ability to discriminate between gestures with similar muscle contractions.

Index terms—3D electrical impedance tomography (EIT), current-steering DAC, hand gesture recognition, machine learning.

I. INTRODUCTION

THE past two decades have seen extensive research efforts on acquiring and decoding physiological signals to drive bionic hands in order to restore lost upper limb functions for amputees and to control robotic arms for human-like hand movement. To achieve close-to-natural bionic hand movements (which include both manipulation of objects and using gestures for supporting communication), reliable signal acquisition methods from which fine details of intention of hand movement can be interpreted are crucial. The most commonly used method to date is surface electromyography (sEMG), where electrical activity produced by skeletal muscles is recorded from electrodes attached to the skin [1] [2]. Despite the advantage of non-invasiveness and being relatively simple to implement, sEMG is limited by its poor spatial resolution, unstable skin-electrode condition and small signal amplitudes from the muscles. Furthermore, sEMG can only detect signals from a depth under the skin of up to 1 cm and provides no access to deep muscles. Implantable electrodes for intramuscular [3], epimysial [4] and intraneural recording [5] can achieve in-depth signal acquisition at higher resolution, but their implementation is limited due to their invasiveness.

Electrical impedance tomography (EIT) has emerged in the past 4-5 years as a potential alternative approach for signal acquisition. EIT detects the inner impedance distribution and
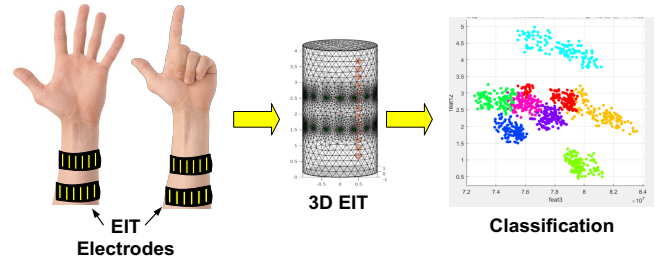

Fig. 1. Conceptual illustration of the proposed 3D EIT approach for hand gesture recognition.

variation of an object by injecting excitation current or voltage in sequence from a group of electrodes around the object, and measures the electrical impedance response from all the electrodes in the group. Because of its advantages including high temporal resolution, non-invasiveness and low-cost implementation, it has been used in clinical applications such as respiratory monitoring [6], [7], [8]. Zhang *et al.* first reported using EIT for hand gesture recognition using an 8-electrode system [9] that was later upgraded to 16 and 32 electrodes [10]. We have also investigated using application-specific integrated circuits (ASIC) based on a high performance EIT system for recognising hand gestures to control a robotic hand [11], [12]. More recently, further research efforts on EIT-based human machine interfaces for hand gesture recognition have been reported including optimising the drive pattern of impedance measurement [13], and using EIT images to interpret grasp force [14]. All the existing research, however, used two-dimensional (2D) EIT systems that map three-dimensional (3D) muscle contraction onto a cross-sectional plane with low spatial resolution, and are prone to detection error. In our earlier study [11], [12], we observed that the detection accuracy was less than 60% when gestures with similar muscle contraction were grouped together for classification but were increased to > 90% after separating these gestures into two groups with a third group as the identifier of the separation.

In this brief we report our investigation on using 3D EIT for hand gesture recognition and its ability to discriminate between gestures with similar muscular contractions. As shown in Fig. 1, 16 electrodes were divided equally into two bands with one near the wrist and the other further up the forearm. We selected eight hand gestures into one group for classification. For comparison, we also tested 2D EIT with the 16 electrodes
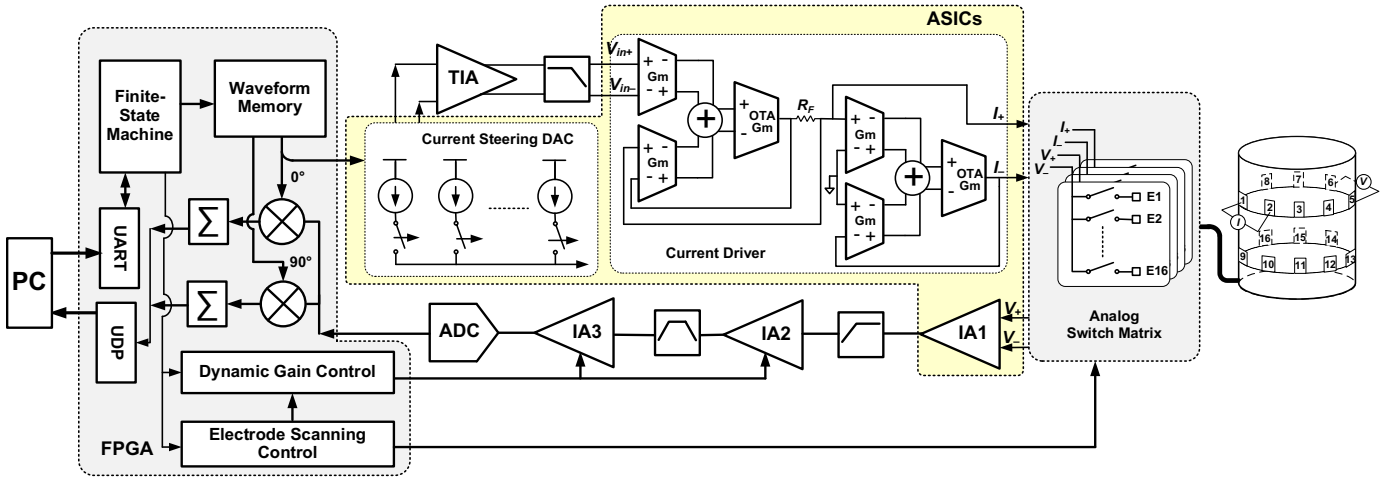
Fig. 2. Architecture of the 16-electrode EIT system.

in one band on the forearm detecting the same eight gestures. The results show that 3D EIT indeed improves the accuracy of recognition, especially for gestures with similar muscle contraction. For these measurements, we have developed a high performance prototype EIT hardware system, featuring an integrated 12-bit current-steering digital-to-analog converter (DAC) with high spectral purity and dynamic gain control for the readout amplifiers, to increase the signal-to-noise ratio in the impedance measurement.

The rest of this brief is organised as follows. Section II describes the hardware implementation. Section III shows the measured results for both the system performance and hand gesture recognition, and conclusions are drawn in Section IV.

II. System Implementation

A. System Architecture

The prototype system hardware shown in Fig.2, comprises an analog front-end for excitation current generation, voltage readout and electrode multiplexing, a digital control unit for system operation control, impedance calculation and communication, and a personal computer (PC) for system configuration and gesture recognition. In this prototype, the analog front-end is based on two ASICs consisting of a wideband fully differential current driver and an instrumentation amplifier, a 12-bit current-steering DAC, and commercial off-the-shelf components. The digital control unit is implemented on a Xilinx Artix-7 FPGA, while MATLAB is used for impedance signal processing and gesture classification.

B. Analog Front-end

In operation, as illustrated in Fig. 2, the 12-bit DAC receives the bitstream of a sinusoidal waveform from the digital control with a sampling rate of 8 MS/s to generate fully differential sinusoidal currents. In the tests the excitation frequency was set to 125 kHz. The differential sinusoidal currents are then converted into differential voltage signals by a transimpedance amplifier (TIA) implemented with AD8056. The voltage signals, V_{in+} and V_{in-}, drive an integrated wideband fully differential current driver to generate the differential excitation currents, I_+ and I_-, with a peak-to-peak amplitude $(I_{+pk} -$

$I_{-pk})$ of 4 mA. The current driver is built with two differential difference transconductance amplifiers (DDTAs) in a source-sink structure [7], where the current amplitude is set by the feedback resistor, R_F, as $I = (V_{in+} - V_{in-})/R_F$. This source-sink combination provides over 97.5% common-mode reduction that minimizes the common-mode error caused by mismatch between the differential currents.

Voltage readout is implemented with three stages of amplification, consisting of an integrated current-feedback instrumentation amplifier IA1, a second stage amplifier IA2 implemented with AD8253 with a programmable gain of 1, 10, 100 and 1000, and IA3 with AD8250 with a programmable gain of 1, 2, 5 and 10. IA1 has a fixed gain of 10, a bandwidth of up to 1 MHz and a common-mode rejection ratio of 74 dB at 1 MHz [7]. The bandpass filter in the readout path has a bandwidth between 65 kHz and 3 MHz to remove interference from the mains, dc offset, and digital operating clocks. The amplified signal is then digitized with a 12-bit analog-to-digital converter (ADC), AD9237, also at a sampling rate of 8 MS/s.

Current and voltage scanning is implemented with an analog switch matrix consisting of 16 ADG1211 chips providing a total of 64 switches, so that each of the two current outputs and two voltage inputs has independent access to the 16 electrodes. This arrangement provides full flexibility when implementing variable impedance measurement sequences [15]. The ADG1211 provides 80 dB of isolation and 90 dB inter-channel isolation that effectively avoids interference due to channel leakage.

C. Current-Steering DAC

To reduce the impedance measurement error caused by the harmonic components in the excitation signal, a random-rotation binary-weighted current steering DAC is implemented. In this way harmonic components in the DAC output caused by the mismatch between the current branches are minimized by randomly selecting current branches, so that distortions due to mismatch are randomized among the sampling cycles [16].

The implementation of the DAC is shown in Fig. 3(a). There are three tiers of current units corresponding to three segments of the 12-bit input; D[11:8], D[7:4] and D[3:0]. Each tier has 15 current units of equal weight. The current unit is
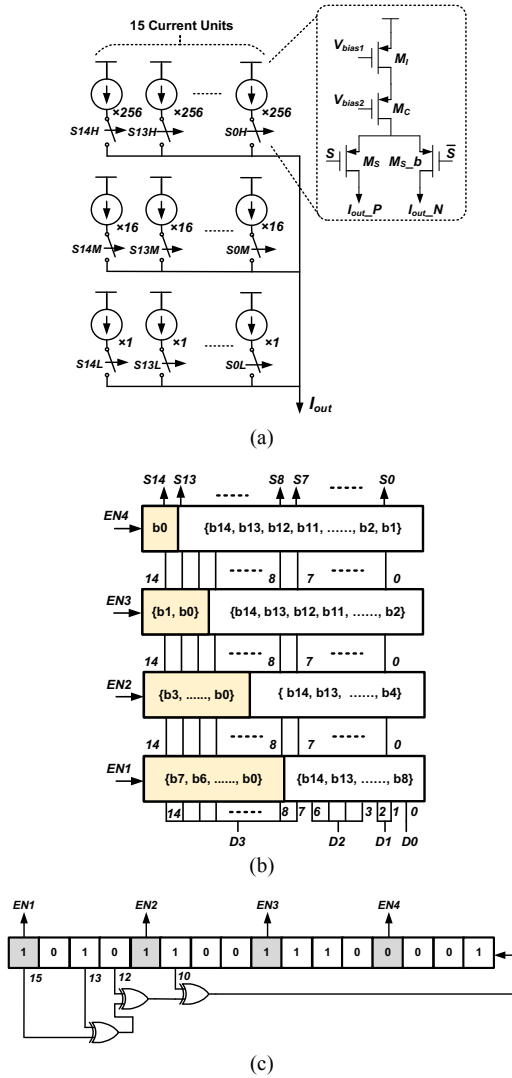
(a)

(b)

(c)

Fig. 3. Implementation of the current-steering DAC: (a) the three-tier architecture of the DAC; (b) cascaded barrel shifters for current unit control in each tier; and (c) 16-bit linear feedback shift register for randomizing the rotation of the barrel shifters.

implemented with a current source transistor M_I, a cascode transistor M_C, and two complimentary switches M_S and M_{S_b} for generating differential current outputs. The weight of transistors of the tier for D[11:8] is 256 times the weight of the tier for D[3:0], while the weight of D[7:3] is 16 times. The differential outputs of the three tiers are summed together to generate the output current with 12-bit resolution. The peak single-end output current value is 2 mA. Fig. 3(b) shows the control of the current units for each tier. At the input, the 4-bit segment in the DAC input is directly expanded to 15 bits, as illustrated, to four 15-bit barrel shifters, which are cascaded together with a rotation step size of 8 bits, 4 bits, 2 bits and 1 bit, respectively, towards the output. Rotation of each register is activated by an enable input. The four enable inputs are generated by a 16-bit linear feedback shift register (LFSR) with an initial value of 16'hACE1, as shown in Fig. 3(c). The LFSR shifts at each sampling clock, generating four pseudorandom enable signals so that the output of the cascaded barrel shifters is randomized among the sampling clocks. Therefore, the
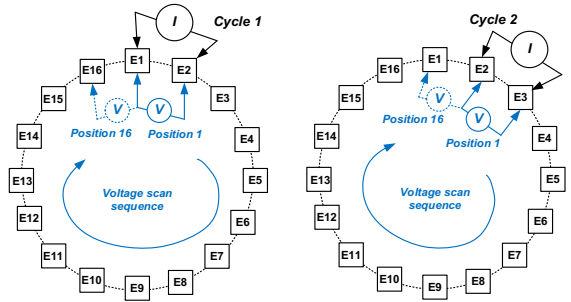

Fig. 4. Illustration of the current injection and voltage scan sequence.

selection of the equally weighted current units in each tier is also randomized.

D. Digital Control

The control logic operates at two clocks; 128 MHz for the serial input to the DAC to achieve an 8 MS/s sampling rate, and 16 MHz for the system operation. The finite-state machine synchronizes for a full impedance scan the output to the DAC, the electrode multiplexing, the sampling of the ADC, and the calculation of the real and imaginary parts of the measured impedance using two parallel multiplier-accumulator units. The calculated values are sent to a PC via 100 MB/s Ethernet using the User Datagram Protocol. The operation of one full scan cycle, including the data transfer, takes 10 ms, when 256 voltage measurements in total are conducted on all the electrode pairs, allowing 32 μs on each electrode pair for voltage sampling and impedance calculation.

For 3D EIT measurements, since the electrodes are separated into two bands the voltage amplitude distribution on the electrode pair has a large variation. Therefore, dynamic gain control is preferable. Fig. 4 shows an example of the impedance measurement sequence. In voltage scan cycle 1, electrodes E1 and E2 are used for current injection, the voltage scan also starts from E1 and E2, and shifts towards E16 by one electrode at a time. In voltage scan cycle 2, the current injection electrodes shift by one to E2 and E3, the voltage scan at this time starts also from E2 and E3, and shifts clockwise towards E1. With this arrangement, in a voltage scan cycle, the distance between the voltage scan and current injection electrode pairs always changes in a fixed pattern, regardless of the location of the current injection. Therefore, the control logic only needs to set 16 different amplifier gains in a voltage scan cycle, and repeat these gain settings for every cycle, instead of storing 256 gain settings for all the 256 measurements.

III. MEASURED RESULTS

A. ASIC Implementation

The current-steering DAC was implemented in XFAB 0.18 μm CMOS technology operating at 1.8 V. Fig. 5 shows the chip micrograph. The DAC occupies an area of 0.26 mm². The fully differential current driver and the current feedback instrumentation amplifier were implemented in XFAB 0.35 μm HV CMOS technology as described in [7]. The entire system is supplied at ±6 V, with an average current consumption of 91 mA in full operation.
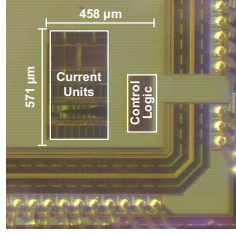
B. DAC Measurements

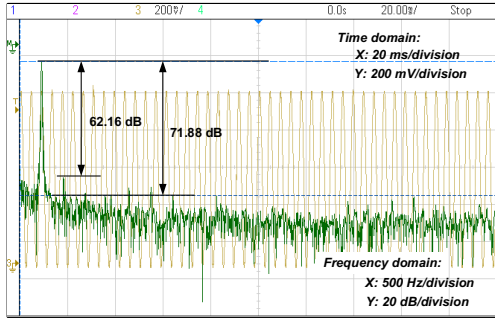Fig. 5. ASIC micrograph of the current-steering DAC.

Fig. 6. Measured output spectrum of the current steering DAC with a sinusoidal output at 244 Hz, a sampling rate of 8 MS/s and 32768 samples per cycle.

The current-steering DAC was tested standalone with its outputs connected to 500 Ω resistor loads. Operating at 128 MHz, the sampling rate was 8 MS/s. A digitized sinusoidal waveform with 12-bit resolution and 32,768 samples per cycle was streamed into the DAC, and the voltage on either load resistors was measured with a Keysight DSO-X 2024A oscilloscope, which also displayed the spectrum of the voltage. Fig. 6 shows a screenshot of the measured voltage and its spectrum with a frequency span of 5 kHz. The output voltage is a sinusoidal waveform with a peak value of 1 V and a frequency of 244 Hz. The measured spurious-free dynamic range (SFDR) in the displayed spectrum is 62.16 dB. This performance is comparable to the commercially available DACs, such as AD5445, which has a wideband SFDR of 62 dB using a 25 MHz clock.

C. Resistive Phantom Measurement

The performance of the 16-electrode EIT system was evaluated with a resistive phantom [17] where inhomogeneity is created by two or four diagonally located switches. Fig. 7 shows the measured EIT images of the 16-electrode system in comparison with images of the 8-electrode system used in our previous study and images from simulation data. The superiority of the 16-electrode system over the 8-electrode system is clearly demonstrated in the figure, where images from the 16-electrode system show a much better match to the simulated images, especially when inhomogeneity was created by all four switches.

D. Hand Gesture Recognition

Eight hand gestures were selected for the recognition tests, namely: *Relax*, *Fist*, *Thumb-Up*, *Left Twist*, *Right Twist*, *Finger Gun*, *Point* and *Scissors*, as illustrated in Fig. 8(a). These eight gestures were tested with two electrode arrangements, one with
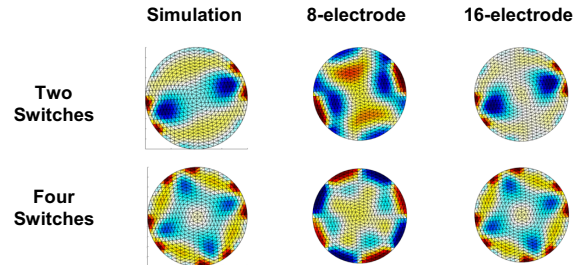

Fig. 7. EIT images created from the outputs o the 8-electrode and 16-electrode systems measuring a resistive phantom, in comparison with images from simulated data.

TABLE I. RECOGNITION ACCURACY OF CLASSIFICATION METHODS

Classification Methods	Accuracy (%)			
		Double Band		
	Single Band	5 cm band separation	10 cm band separation	10 cm band separation with 40 dB THD
Decision Tree:				
Fine Tree	97.9	99.5	96.6	80.1
Medium Tree	95.4	99.5	93	65.2
SVM:				
Quadratic	97.5	99.4	97.4	82.9
Cubic	95.1	99	96.7	82.5
Medium Gaussian	88.2	95.9	93	73.2
ANN	95.4	99.5	97.7	87.4

the 16 electrodes on a single wristband for 2D EIT measurement, and the other with the same number of electrodes divided equally between the two bands and worn as illustrated in Fig. 1, for 3D EIT measurement. Sixteen nickel-plated steel plates, 25 mm × 5 mm each, attached on elastic bands, were used as electrodes in the tests, while Spectra 360 electrode gel (Parker Laboratories, Inc) was applied to improve contact conductivity. Two volunteers were recruited. Sixty five rounds of tests, each consisting of all the eight gestures, were performed. 5,750 full scan cycles, namely frames, were recorded consisting of in total 1,472,000 voltage measurements, 184,000 for each gesture. The acquisition speed was 33 frames/s. In 3D EIT measurements, the two electrode bands were placed with a separation of either 5 cm or 10 cm. For all measurements, the excitation signal was a 125 kHz single frequency sinusoidal current. In addition, five rounds of 3D EIT measurements at 10 cm band separation with added distortion of 40 dB total harmonic distortion (THD) introduced in the DAC input.

The MATLAB R2019b Classification Learner APP was used for data analysis. The Fine-Tree classification method was employed and five-fold cross-validation was performed. For either electrode arrangement, datasets from each gesture were equally divided into five groups, where four groups were used for training and the remaining group for validation, and the accuracy was calculated after five rounds of iterations of changing groups for training and validation.

Fig. 8(b) shows the confusion matrix of the single band 2D EIT recognition. As shown, the eight gestures are classified with an average of 97% accuracy. While other gestures are generally well classified, most of the confusion, as shown in
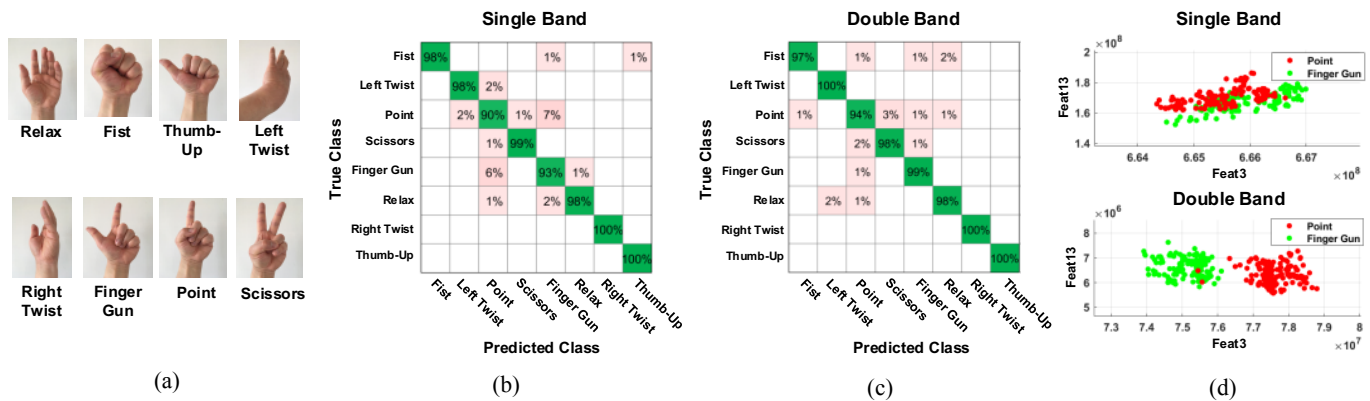
Fig. 8. Hand gesture recognition results: (a) hand gestures used in tests; (b) confusion matrix of recognition using 2D EIT single wristband electrode arrangement; (c) confusion matrix using 3D EIT with double wristband electrode arrangement; and (d) comparison between 2D and 3D EIT of the clustering feature space of two gestures.

pink pixels, is observed between the *Finger Gun* and *Point*, which reflects the similarity in the muscle contraction for these gestures. Fig. 8(c) shows the confusion matrix of the double band 3D EIT recognition. With the same classifier and settings, improvement is clearly observed with the average accuracy increased to 98.25%. The confusion between the *Finger Gun* and *Point* is significantly reduced. Fig. 8(d) compares the clustering between the *Finger Gun* and *Point* in a feature space with 2D and 3D EIT recognition. Clearly 3D EIT demonstrates better clustering discrimination.

In addition to the Fine Tree method, datasets from the eight gestures were also tested with other decision trees and support vector machine (SVM) algorithms available in the Classification Learner APP, as well as the artificial neural network (ANN) algorithm with 10 hidden neurons. The classification accuracy from each algorithm is listed in Table I. In general, 3D EIT demonstrates better recognition accuracy than 2D EIT, while closer placement of the electrode bands yields higher accuracy from all classification methods, possibly because of higher signal-to-noise ratio when the excitation and acquisition are on separated bands. The measured effect of harmonic distortion on accuracy emphasizes the importance of a high-performance excitation signal source.

IV. CONCLUSION

In this brief we have presented a prototype 16-electrode EIT system with an integrated current-steering DAC that provides high spectral purity of the excitation signal for impedance measurements. We have also reported our investigation of hand gesture recognition using this system with both 2D and 3D EIT electrode arrangements. The results show improved overall recognition accuracy of 99.5% when all the gestures under test were classified as one group, compared to the $< 60\%$ accuracy in our previous study [11], thanks to the advanced EIT hardware and higher resolution provided by more electrodes. Moreover, our investigation has demonstrated the advantage of using 3D EIT for hand gesture recognition, especially in discriminating gestures with similar muscle contraction.

REFERENCES

[1] D. Farina, N. Jiang, H. Rehbaum, A. Holobar, B. Graimann, H. Dietl and O. C. Aszmann, "The extraction of neural information from the surface EMG for the control of upper-limb prostheses: Emerging avenues and challenges," *IEEE Trans. Neural Syst. Rehabil. Eng.*, vol. 22, no. 4, pp. 797 - 809, July 2014.

[2] W. Geng, Y. Du, W. Jin, W. Wei, Y. Hu and J. Li, "Gesture recognition by instantaneous surface EMG images," *Scientific Reports*, vol. 6, no. 36571, pp. 1-8, 2016.

[3] R. F. Weir, P. R. Troyk, G. A. DeMichele, D. A. Kerns, J. F. Schorsch and H. Maas, "Implantable myoelectric sensors (IMESs) for intramuscular electromyogram recording," *IEEE Trans. Biomed. Eng.*, vol. 56, no. 1, pp. 159-171, Jan. 2009.

[4] S. Lewis et al., "Fully implantable multi-channel measurementSystem for acquisition of muscle activity," *IEEE Trans. Instrum. Meas.*, vol. 62, no. 7, pp. 1972 - 1981, July 2013.

[5] T. Boretius, J. Badia, A. Pascual-Font, M. Schuettler, X. Navarro, K. Yoshida and T. Stieglitz, "A transverse intrafascicular multichannel electrode (TIME) to interface with the peripheral nerve," *Biosens. Bioelectron.*, vol. 26, no. 1, pp. 62-69, Sept. 2010.

[6] Y. Wu, D. Jiang, A. Bardill, S. de Gelidi, R. Bayford and A. Demosthenous, "A high frame rate wearable EIT system using active electrode ASICs for lung respiration and heart rate monitoring," *IEEE Trans. Circuits Syst. I: Regular Papers*, vol. 65, no. 11, pp. 3810 - 3820, Nov. 2018.

[7] Y. Wu, D. Jiang, A. Bardill, R. Bayford and A. Demosthenous, "A 122 fps, 1 MHz bandwidth multi-frequency wearable EIT belt featuring Novel active electrode architecture for neonatal thorax vital sign monitoring," *IEEE Trans. Biomed. Circuits Syst.*, vol. 13, pp. 927 - 937, Oct. 2019.

[8] M. Kim, J. Jang, H. Kim, J. Lee, J. Lee, J. Lee, K.-R. Lee, K. Kim, Y. Lee, K. J. Lee and H.-J. Yoo, "A 1.4-m Ω -sensitivity 94-dB dynamic-range electrical impedance tomography SoC and 48-channel hub-SoC for 3-D lung ventilation monitoring System," *IEEE J. Solid-State Circuits*, vol. 52, no. 11, pp. 2829 - 2842, Nov. 2017.

[9] Y. Zhang and C. Harrison, "Tomo: Wearable, low-Cost, electrical impedance tomography for hand gesture recognition," *in Proc. 28th Ann. ACM Symp. User Interface Software & Technology (UIST'15)*, Nov. 2015.

[10] Y. Zhang, R. Xiao and C. Harrison, "Advancing hand gesture recognition with high resolution electrical impedance tomography," *in Proc. 29th Ann. Symp. User Interface Software & Technology (UIST '16)*, Oct. 2016.

[11] Y. Wu, D. Jiang , J. Duan, X. Liu, R. Bayford and A. Demosthenous, "Towards a high accuracy wearable hand gesture recognition system using EIT," *in Proc. 2018 IEEE Int. Symp. Circuits Syst. (ISCAS)*, Florence, Italy , 27-30 May 2018.

[12] Y. Wu, D. Jiang, X. Liu, R. Bayford and A. Demosthenous, "A human–machine interface using electrical impedance tomography for hand prosthesis control," *IEEE Trans. Biomed. Circuits Syst.*, vol. 12, no. 6, pp. 1322 - 1333, Dec. 2018.

[13] G. Ma, Z. Hao, X. Wu and X. Wang, "An optimal electrical impedance tomography drive pattern for human-computer interaction applications," *IEEE Trans. Biomed. Circuits Syst.*, Early Access, pp. 1-10, 20 Jan. 2020.

[14] E. Zheng, Y. Li, Q. Wang and H. Qiao, "Toward a human-machine interface based on electrical impedance tomography for robotic manipulator control," *in 2019 IEEE/RSJ Int. Conf. Intelligent Robots and Systems (IROS)*, Macau, China, Nov. 4-8, 2019.

[15] S. Russo, S. Nefti-Meziani, N. Carbonaro and A. Tognetti, "A quantitative evaluation of drive pattern selection for optimizing EIT-based stretchable sensors," *Sensors*, vol. 17, no. 9, p. 1999, 2017.

[16] W.-T. Lin and T.-H. Kuo , "A compact dynamic-performance-improved current-steering DAC with random rotation-based binary-weighted selection," *IEEE J. Solid-State Circuits*, vol. 47, no. 2, pp. 444 - 453, Feb. 2012.

[17] S. AG, "Swisstom EIT Resistor Mesh Phantom 32-HG User Manual 1ST504-103," June 2013. [Online]. Available: http://www.swisstom.com/software/PDF/ResistorPhantomManual_1ST504-103_Rev_000.pdf.